Electronic Supplementary Information

Effect of regulating the interfacial structure of multiple non-covalent bonding on improving thermal management capability

Xu Li,[a] Bin Wu,*[a] Ying Lv,[b] Ru Xia,[a] Jiasheng Qian*[a]

[a] Key Laboratory of Environment-Friendly Polymeric Materials of Anhui Province, School of Chemistry & Chemical Engineering, Anhui University, Hefei, Anhui, 230601, China;

[b] Department of Chemistry and Centre for Atomic Engineering of Advanced Materials, Anhui Province Key Laboratory of Chemistry for Inorganic/Organic Hybrid Functionalized Materials, Key Laboratory of Structure and Functional Regulation of Hybrid Materials of Ministry of Education, Anhui University, Hefei, Anhui, 230601, China.

* Corresponding authors.

E-mail addresses: lwbin@ahu.edu.cn (B. Wu), qianjsh@ahu.edu.cn (J. Qian)

Characterizations.

X-ray diffractometer (XRD, Rigaku, SmartLab, Japan) measurement was used to analyze the crystal structure of samples. Fourier transform infrared spectroscopy (FTIR, Bruker, TG209F3, Germany) were carried out to analyze functional group of samples. X-ray photoelectron spectroscopy (XPS, Thermo Scientific, Escalab 250Xi, England) was performed to characterize the chemical structure of samples. The morphology of samples was using a scanning electron microscope (SEM, Hitachi, S-4800, Japan and Zeiss, Sigma 500, Germany), atomic force microscopy (AFM, Hitachi, AFM5500M, Japan), and transmission electron microscopy (TEM, JEOL, JEM-2100, Japan). Raman spectrum were conducted by in micro-raman spectroscopy (Via-Reflex, Renishaw, England). Energy dispersive X-ray spectroscopy (EDS) was used to conduct the element analysis of the sample. The oriented structure of composite was analyzed by 2D Wide-angle X-ray scattering (2D WAXS, Xenocs, Xuess3.0, France). The Zeta potential of the samples was characterized by nano laser particle size meter (Malvern, Zetasizer Nano-zs90, England). The contact angles and the surface tensions of samples were measured by optical contact angle measuring instrument (Kruss, DSA30S, Germany). Thermogravimetric analysis was tested the content of IL for modifying BNNS (TGA, Setaram, Labsys evo, France). The mechanical properties of composite were characterized on a universal material testing machine (Instron 5967, USA). Temperature distribution images of the composites were obtained via an infrared thermograph (FLIR Systems, FLIR T1040, USA). Volume resistivity was measured by automatic resistance measuring instrument (GEST-121A, China). The limited oxygen

index was measured by an oxygen index meter (Nanjing Shangyuan HC-2CZ, China). Total heat release (THR) and peak heat release rate (PHRR) were characterized by microscale combustion calorimeter (MCC-3, Deatak, USA).

The in-plane thermal conductivities ($\kappa_{\parallel}$) were obtained by the equation

$$\kappa_{\parallel} = \alpha_{\parallel} \times C_p \times \rho \quad \text{(S1)}$$

where $\alpha_{\parallel}$, C_p and ρ respectively correspond to in-plane thermal diffusivity, specific heat capacity, and density. The $\alpha_{\parallel}$ and C_p were measured using a Netzsch LFA 467 and a TA Q2000 Instruments, respectively. ρ was achieved by the ratio of the mass and volume of the sample.

Calculated surface energy

$$\gamma_{sl} = \gamma_{sg} - \gamma_{lg}\cos\theta \quad \text{(S2)}$$

where γ_{sl}, γ_{sg}, γ_{lg}, and θ are solid-liquid interfacial energy of BNNS and H_2O (or IL solution), solid-gas interfacial energy of BNNS and air, liquid-gas interfacial energy of H_2O (or IL solution) and air, and equilibrium contact angle of liquid on the solid surface, respectively. γ_{lg} and θ were obtained from measurements of surface tension and contact angle from Fig. S2 and Fig. 2a, respectively. γ_{sg} is calculated by the formula (S3) [1].

$$\gamma_{sg} = \gamma_{sg}^{d} + \gamma_{sg}^{p} \quad \text{(S3)}$$

where γ_{sg}^{d} and γ_{sg}^{p} are the dispersive and polar components of the surface energy for BNNS and air. γ_{sg}^{d} and γ_{sg}^{p} are calculated by Wu's equation (S4) [2].

$$\gamma(\cos\theta + 1) = 4\left(\frac{\gamma^{d}\gamma_{sg}^{d}}{\gamma^{d} + \gamma_{sg}^{d}} + \frac{\gamma^{p}\gamma_{sg}^{p}}{\gamma^{p} + \gamma_{sg}^{p}}\right) \quad \text{(S4)}$$

where γ is the total surface energy, and γ^d and γ^p are the dispersive and polar components of the surface energy, respectively (Table S1). θ is contact angle.

$$\begin{cases} \gamma_{H2O}\left(\cos\theta_{H2O}+1\right) = 4\left(\dfrac{\gamma_{H2O}^{d}\gamma_{sg}^{d}}{\gamma_{H2O}^{d}+\gamma_{sg}^{d}}+\dfrac{\gamma_{H2O}^{p}\gamma_{sg}^{p}}{\gamma_{H2O}^{p}+\gamma_{sg}^{p}}\right) \\ \gamma_{glycerol}\left(\cos\theta_{glycerol}+1\right) = 4\left(\dfrac{\gamma_{glycerol}^{d}\gamma_{sg}^{d}}{\gamma_{glycerol}^{d}+\gamma_{sg}^{d}}+\dfrac{\gamma_{glycerol}^{p}\gamma_{sg}^{p}}{\gamma_{glycerol}^{p}+\gamma_{sg}^{p}}\right) \end{cases}$$

where γ_{H2O} and $\gamma_{glycerol}$were the total surface energy of H_2O and glycerol. γ_{H2O}^{d} and γ_{H2O}^{p} are the dispersive and polar components of the surface energy for H_2O. $\gamma_{glycerol}^{d}$ and $\gamma_{glycerol}^{p}$ are the dispersive and polar components of the surface energy for glycerol (Table S1). θ are contact angles of water and glycerol on the surface of FL-BNNS (Fig. S3).

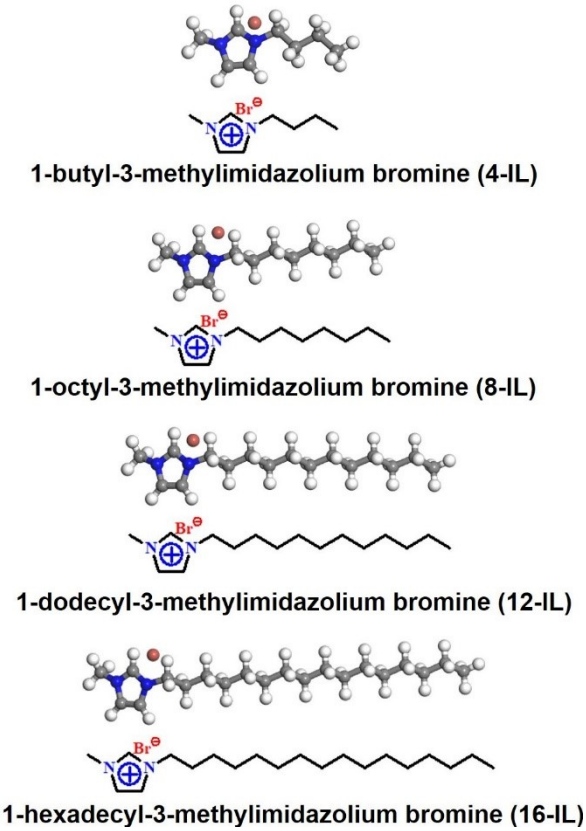

Fig. S1 Imidazolium ionic liquids with different carbon chain structures.

Table S1 Surface tension of water and glycerin

Liquids	**γ (mJ·m^{-2})**	**γ^{d} (mJ·m^{-2})**	**γ^{p} (mJ·m^{-2})**
H_2O	72.8	21.8	51.0
glycerol	63.4	37.0	26.4

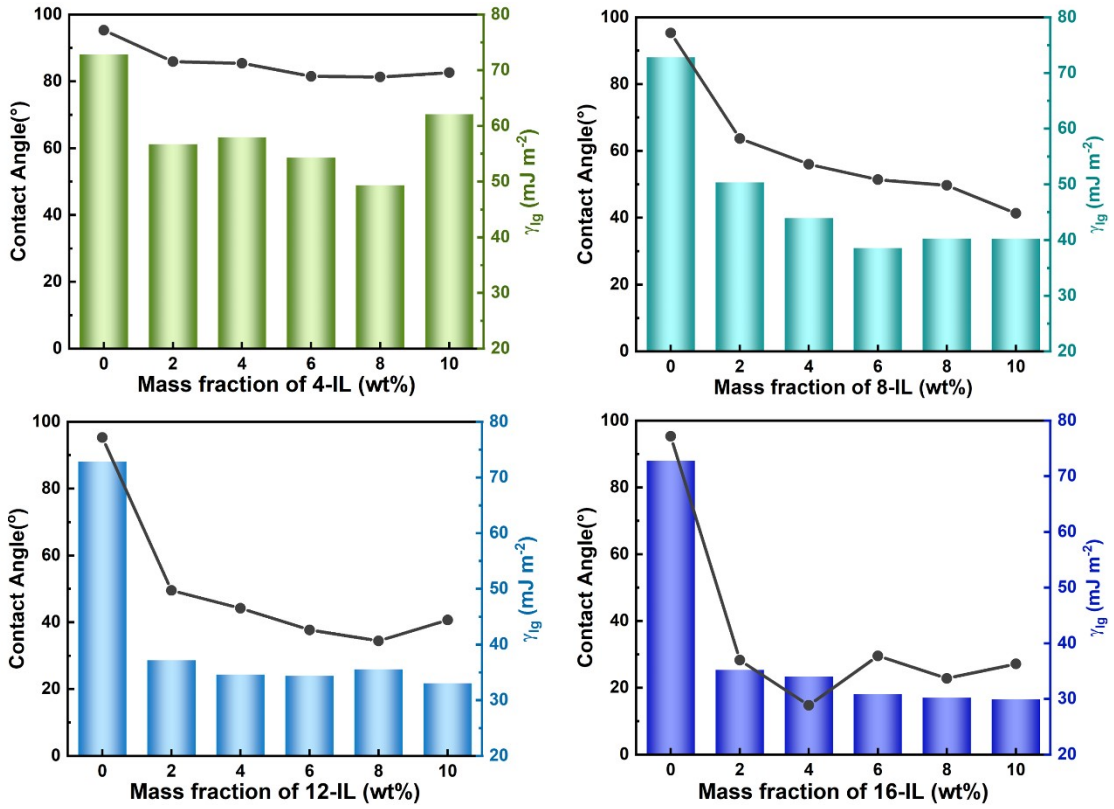

Fig. S2 The contact angle and surface tension as the function of the mass fraction of IL with different side carbon chain lengths.

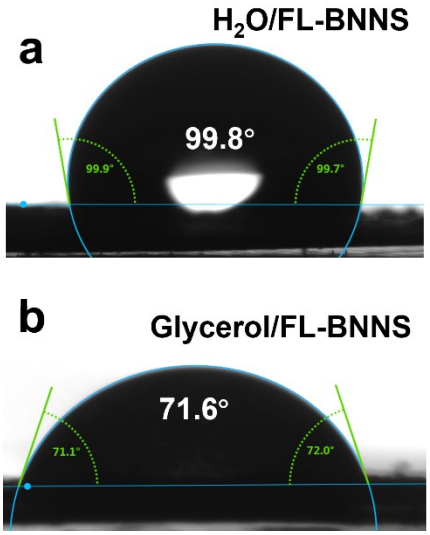

Fig. S3 Contact angles of H_2O and glycerol on the surface of FL-BNNS, respectively.

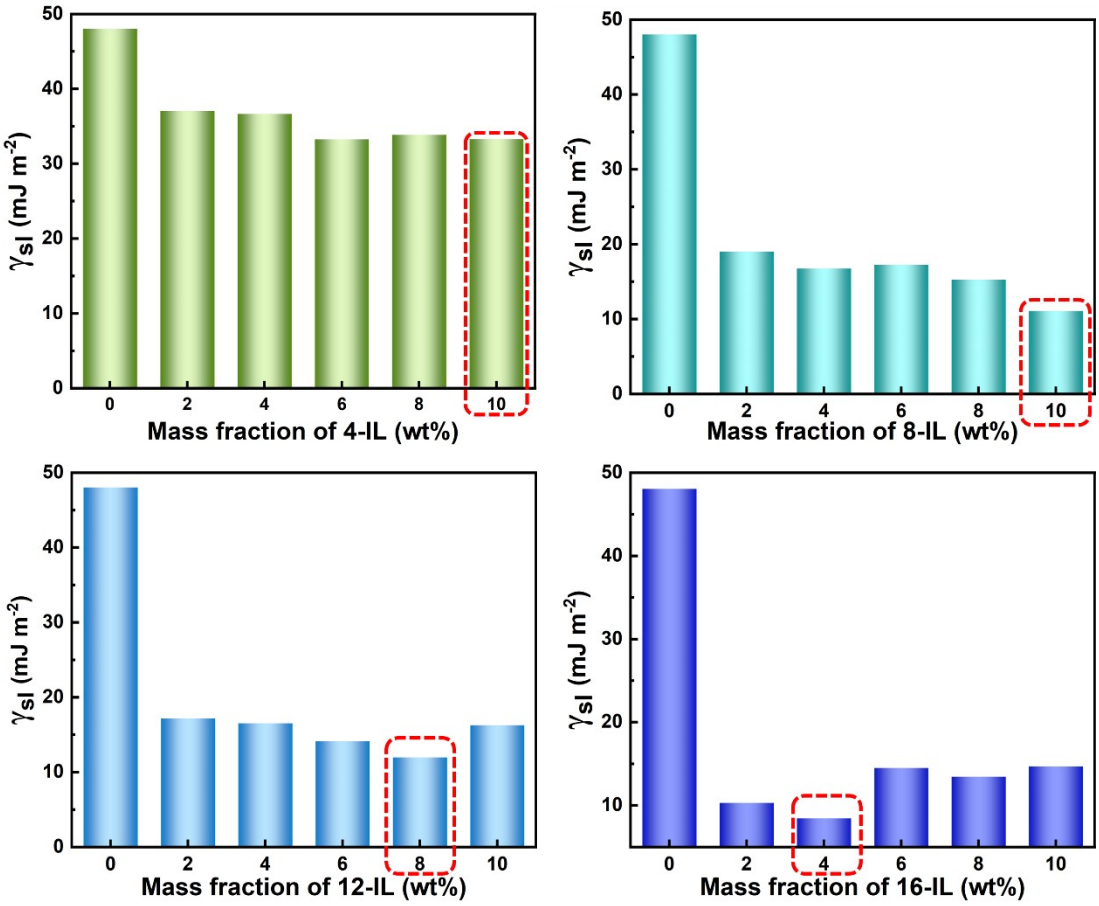

Fig. S4 The solid-liquid surface energy as a function of the mass fraction of IL with different side carbon chain lengths.

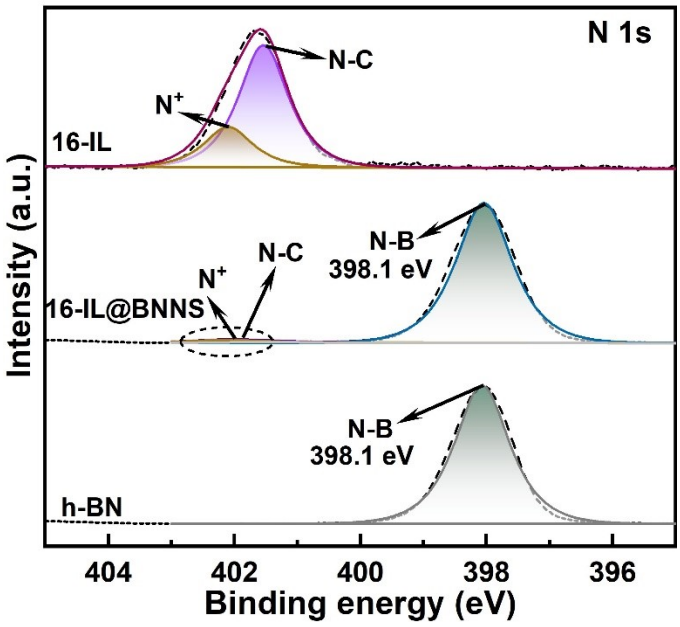

Fig. S5 N 1s XPS spectra of 16-IL, h-BN, and 16-IL@BNNS.

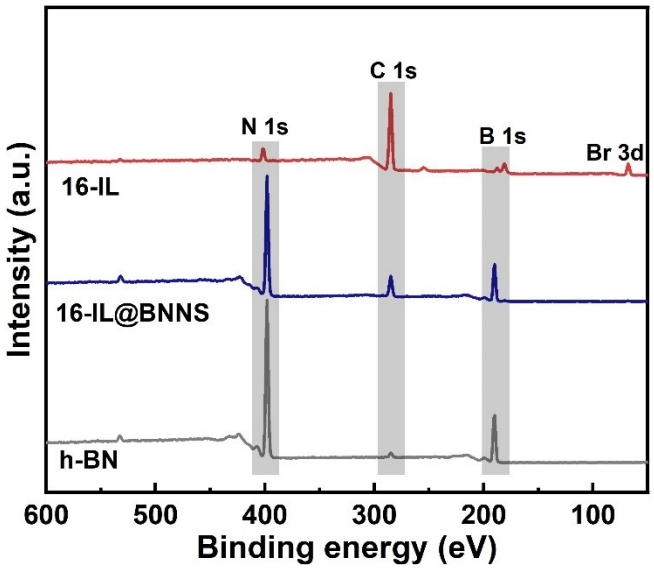

Fig. S6 XPS full spectra of h-BN, 16-IL, and 16-IL@BNNS, respectively.

Table S2 Comparison of atomic concentration of C, N, and B in h-BN and 16-IL@BNNS by the XPS full spectrums.

Samples	Atomic concentration (%)			N/B atomic ration	N/C atomic ration
	C 1s	N 1s	B 1s		
h-BN	2.30	44.3	52.4	0.85	19.3
16-IL@BNNS	12.1	39.5	46.8	0.84	3.26

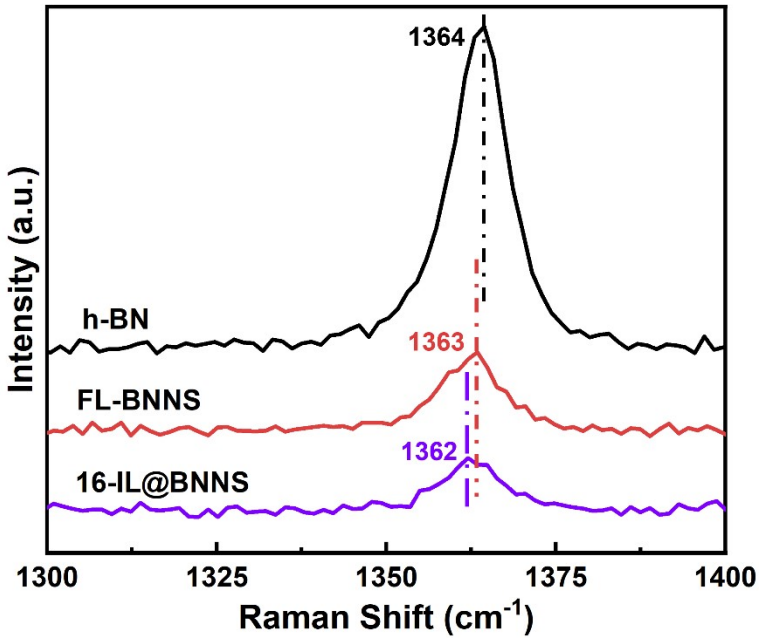

Fig. S7 Raman of h-BN, FL-BNNS, and 16-IL@BNNS, respectively.

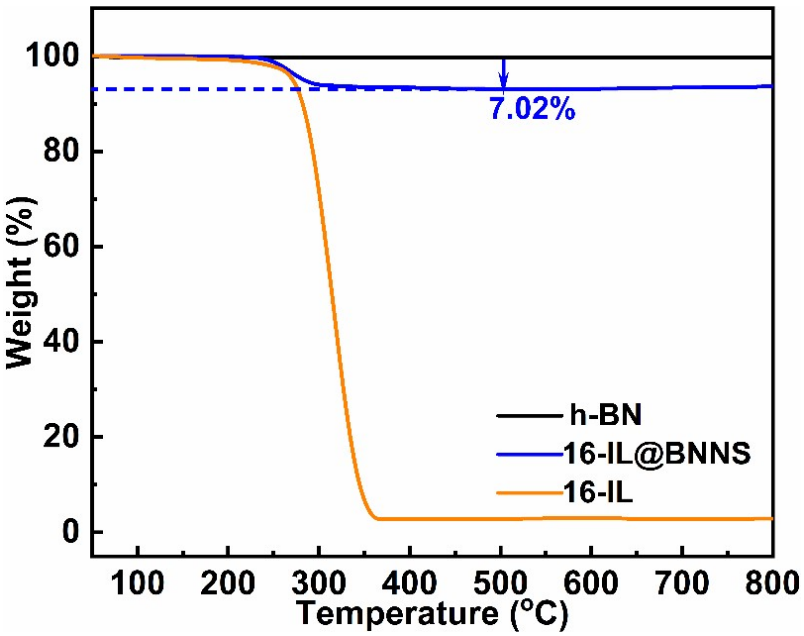

Fig. S8 TGA of 16-IL, h-BN, and 16-IL@BNNS, respectively.

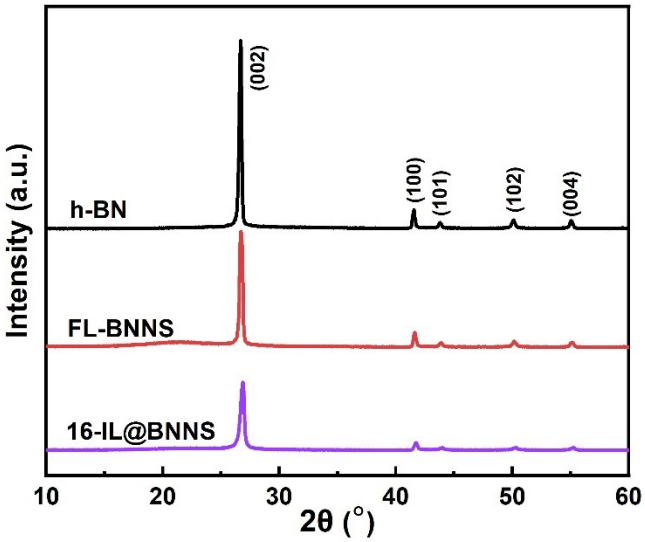

Fig. S9 XRD patterns of h-BN, FL-BNNS, and 16-IL@BNNS, respectively.

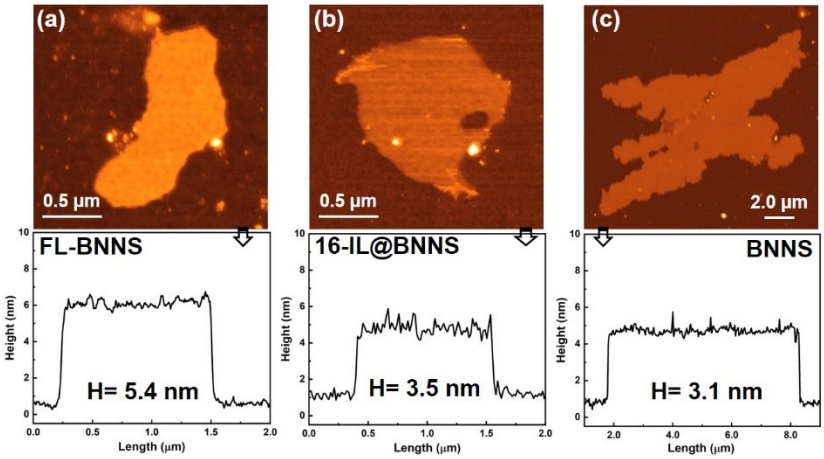

Fig. S10 AFM topographic image of (a) FL-BNNS, (b) 16-IL@BNNS, and (a)BNNS and curves of surface scale.

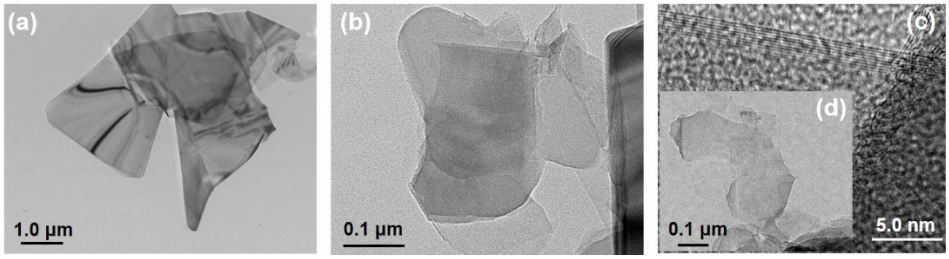

Fig. S11 TEM of (a) FL-BNNS, (b) 16-IL@BNNS, and (d) BNNS, HRTEM of (c) BNNS.

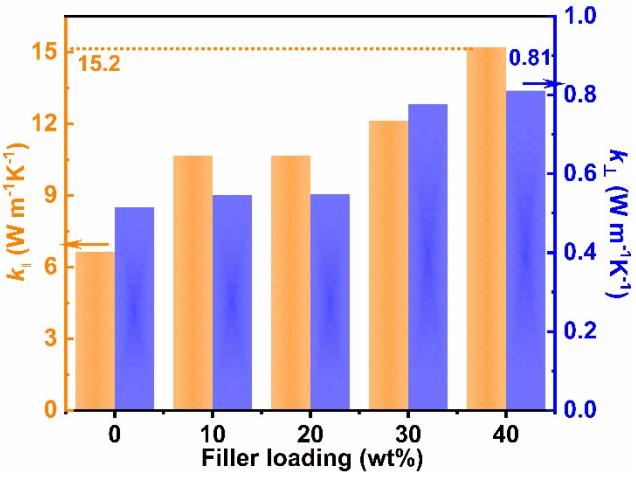

Fig.S12 $k_{\parallel}$ and $k_{\perp}$ of 16-IL@BNNS/ANF with different filler loading.

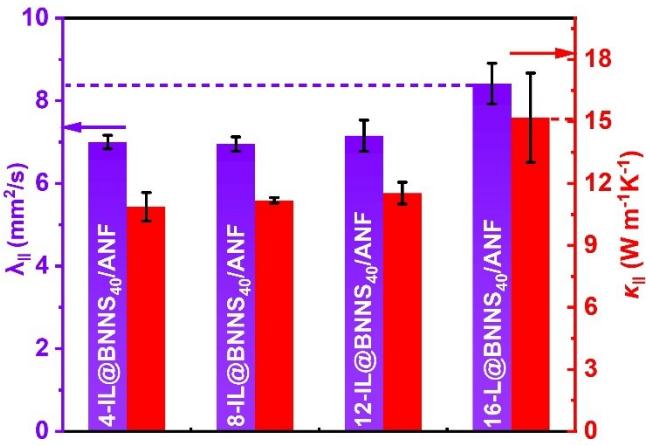

Fig. S13 $\lambda_{\parallel}$ and $k_{\parallel}$ of y-IL@$BNNS_{40}$/ANF (y=4, 8, 12, and 16, the number of carbon atoms in the alkyl chain).

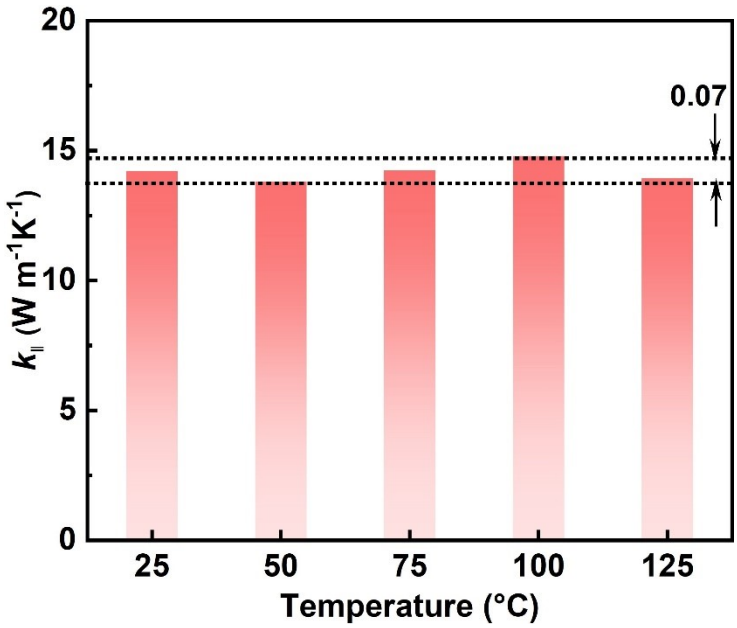

Fig. S14 Relationship between temperature and thermal conductivity of 16-IL@BNNS/ANF.

Table S3 Thermal conductivity (TC) of BNNS-based composites at room temperature

Materials	Loading	TC (W m^{-1} K^{-1})	Interface structure	References
BNNS/PVDF	60 wt%	11.88	none	[3]
MVQ/ABN	54 vol%	6.34	none	[4]
Wax-BNNS	50 wt%	3.47	none	[5]
PVDF/BNNS	4 wt%	4.69	covalent bond	[6]
APTES-BNNS/EP	40 wt%	5.86	covalent bond	[7]
f-BNNS/SCLCP	30 wt%	2.46	covalent bond	[8]
BNNS/EVA	50 wt%	13.2	van der Waals	[9]
NF-BNNS/PMMA	80 wt%	10.2	physical adsorption	[10]
CNFs/BNNS-p-APP	33.3 wt%	9.10	electrostatic interaction	[11]
Epoxy/3D-C-BNNS	9.6 vol%	3.12	hydrogen bond	[12]
LS0.2-BN/CNF/CNF	50 wt%	1.22	hydrogen bond	[13]
PVA/30BP-2.7BNNS	31.92 wt%	9.45	hydrogen bond	[14]
m-BN/PVDF	40 wt%	6.50	π-π	[15]
BNNS@PDA/ANF	50 wt%	3.94	π-π	[16]
PEI/(PI-BN)	60 wt%	3.3	π-π	[17]
PVA/BNNS-PDA-Ag/GO	14 wt%	7.04	π-π	[18]
BNNS/HBPE@PSF	40 wt%	3.28	CH-π and π-π	[19]
BNNS/PVA	92.5 wt%	12.2	cation-π	[20]
BNNS/Si-GFs/E-44	15 wt%	2.75	cation-π	[21]
16-IL@$BNNS_{40}$/ANF	40 wt%	15.2	cation-π and CH-π	This work

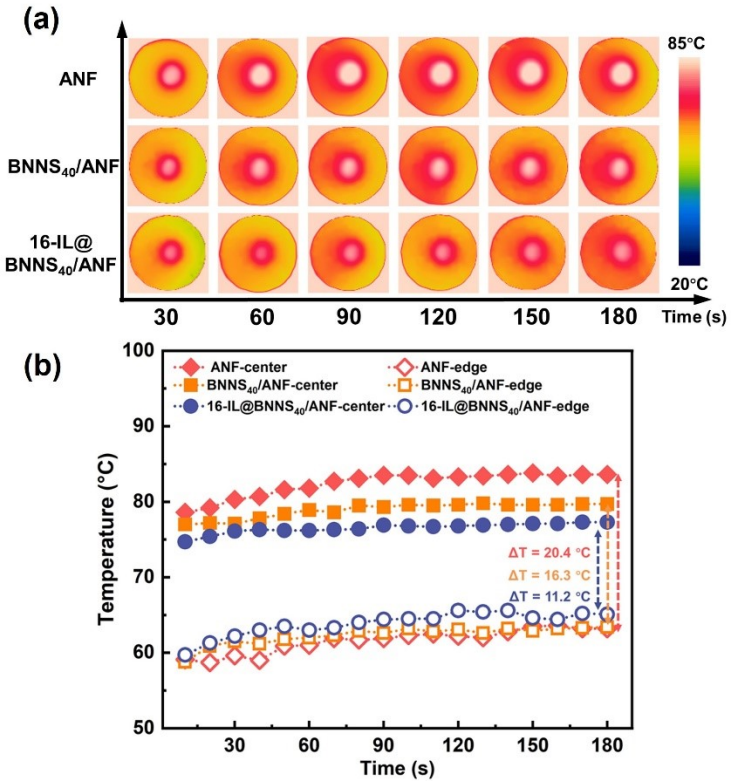

Fig. S15 (a) The infrared thermal images and (b) the central point and edge temperatures curves of ANF, $BNNS_{40}$/ANF, and 16-IL@$BNNS_{40}$/ANF at different times, respectively.

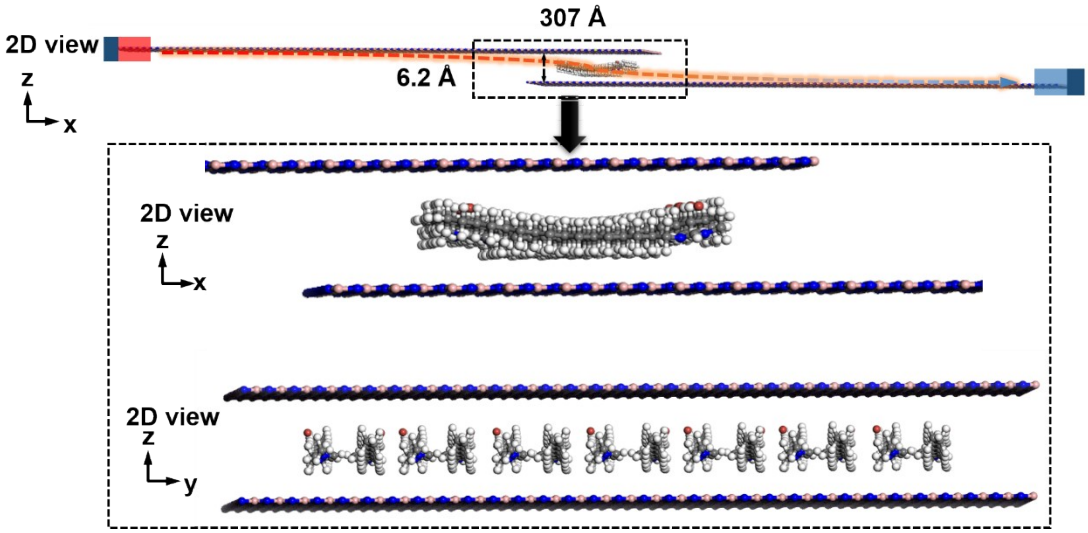

Fig. S16 Simulation modeling of IL_{16}@BNNS.

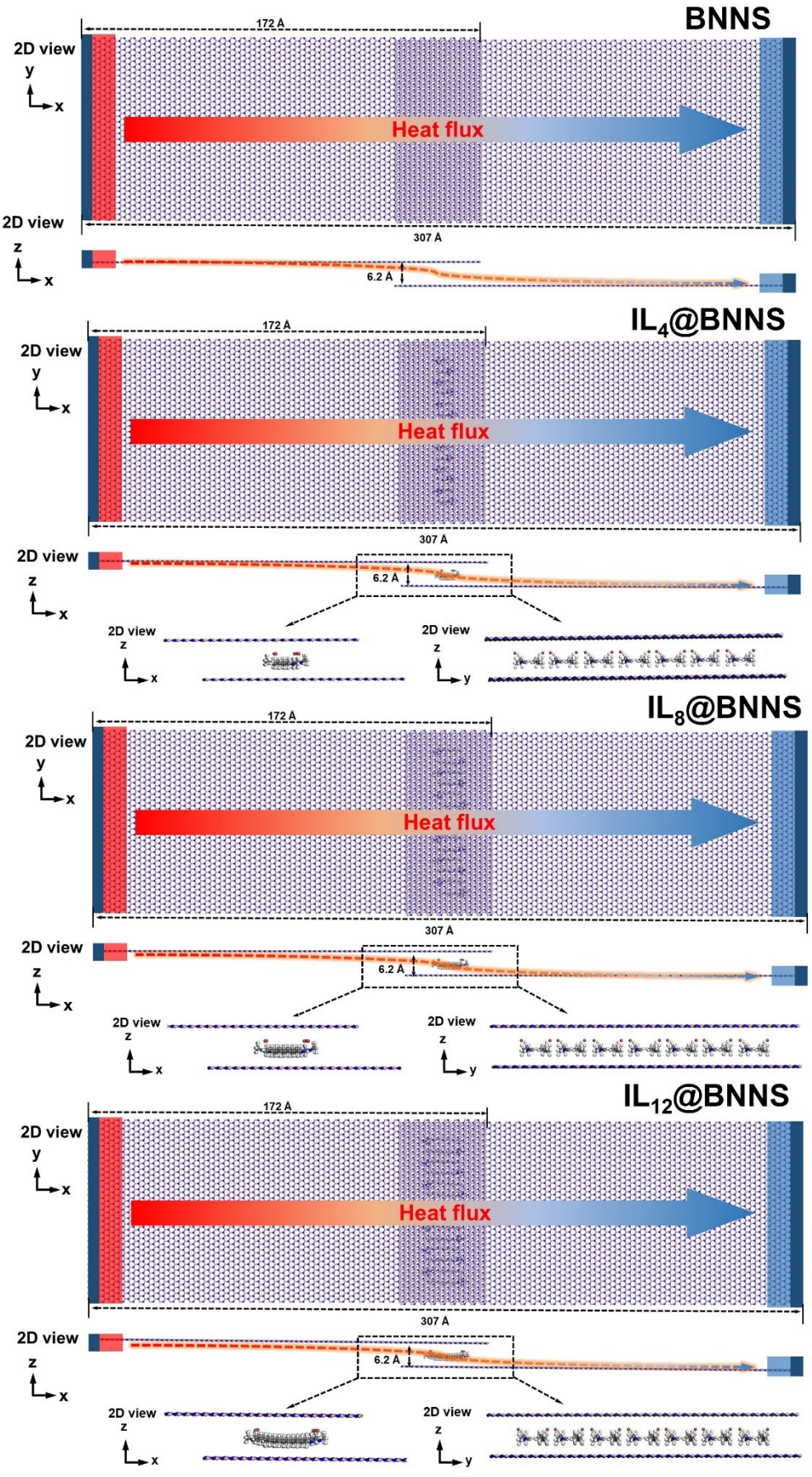

Fig. S17 Simulation modeling of BNNS, IL_4@BNNS, IL_8@BNNS, and IL_{12}@BNNS, respectively.

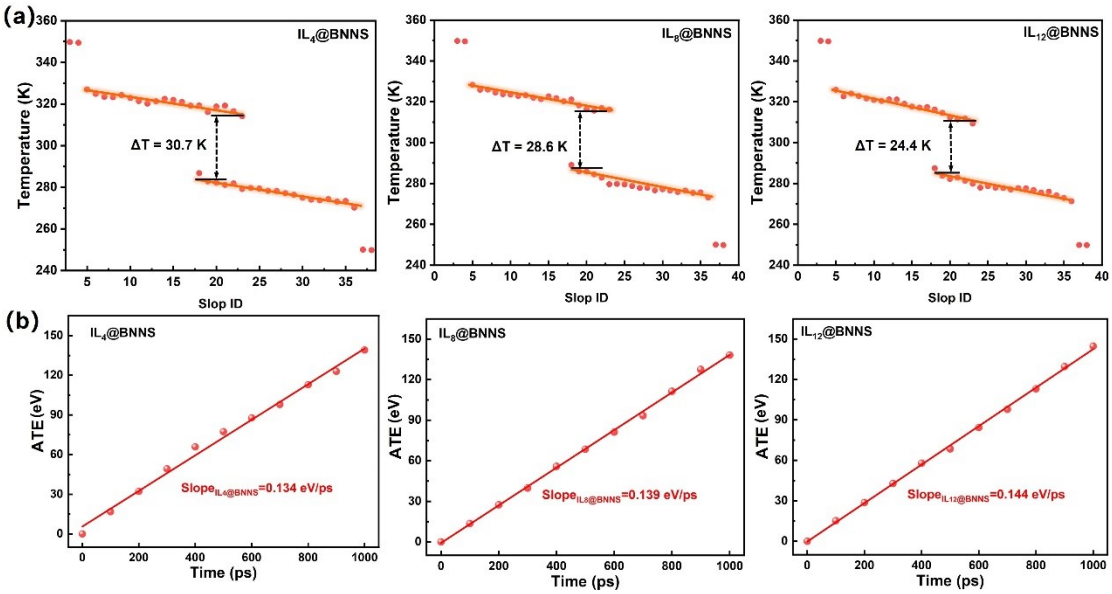

Fig. S18 (a) Steady-state temperature profile of IL_4@BNNS, IL_8@BNNS and IL_{12}@BNNS obtained using the NEMD.

(b) ATE as a function of the time in steady state for IL_4@BNNS, IL_8@BNNS and IL_{12}@BNNS, respectively.

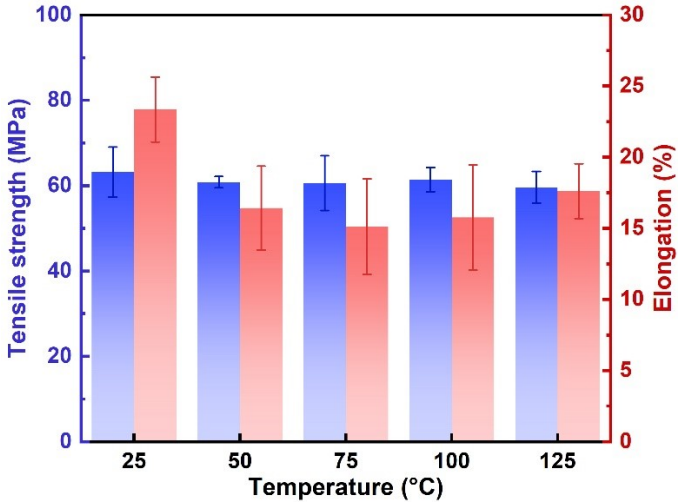

Fig. S19 Mechanical properties of 16-IL@BNNS$_{40}$/ANF with temperature variation.

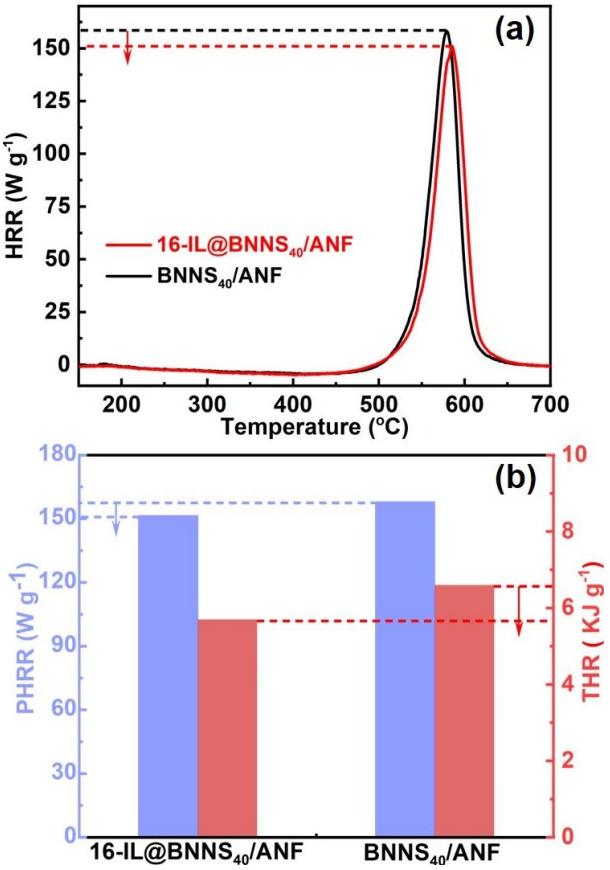

Fig. S20 (a) Heat release rate curves and (b) PHRR and THR values of 16-IL@$BNNS_{40}$/ANF and $BNNS_{40}$/ANF.

Fig. S21 Digital image of 16-IL@BNNS/ANF on setaria viridis.

Reference

[1] S. H. Wu, K. J. Brzozowski, J Colloid Interface Sci., 1971, **37**, 686-690.

[2] D. Liu, B. Liu, C. Wang, W. Jin, Q. Zha, G. Shi, D. Wang, X. Sang, C. Ni, ACS Sustain. Chem. Eng., 2020, **8**, 2167-2175.

[3] C. Teng, L. Su, J. Chen, J. Wang, Compos. Part A Appl. Sci. Manuf., 2019, **124**, 105498.

[4] Z. H. Yin, J. H. Guo, X. H. Jiang, Compos. Sci. Technol., 2021, **209**, 108794.

[5] Z. Yang, L. H. Zhou, W. Luo, J. Y. Wan, J. Q. Dai, X. G. Han, K. Fu, D. Henderson, B. Yang, L. B. Hu, Nanoscale, 2016, **8**, 19326-19333.

[6] M. Wang, Z. Jiao, Y. Chen, X. Hou, L. Fu, Y. Wu, S. Li, N. Jiang, J. Yu, Compos. Part A Appl. Sci. Manuf., 2018, **109**, 321-329.

[7] Z. Liu, J. Li, X. Liu, ACS Appl. Mater. Interfaces, 2020, **12**, 6503-6515.

[8] X. L. Zheng, Y. J. Zhan, J. Shi, M. E. Lu, K. Wu, Nanoscale, 2023, **15**, 13025-13036.

[9] Z.-G. Wang, W. Liu, Y.-H. Liu, Y. Ren, Y.-P. Li, L. Zhou, J.-Z. Xu, J. Lei, Z.-M. Li, Compos. B. Eng., 2020, **180**, 107569.

[10] T. Morishita, H. Okamoto, ACS Appl. Mater. Interfaces, 2016, **8**, 27064-27073.

[11] D. Hu, H. Liu, Y. Ding, W. Ma, Carbohydr. Polym., 2021, **264**, 118058.

[12] J. Chen, X. Huang, Y. Zhu, P. Jiang, Adv. Funct. Mater., 2017, **27**, 1604754.

[13] X. Wang, M. Sun, R. Wang, L. Jiao, H. Bian, H. Dai, Mater. Des., 2022, **214**, 110379.

[14] J. J. Hu, T. R. Zhang, L. L. Wang, Z. Q. Shi, H. Y. Xia, ACS Appl. Mater. Interfaces, 2023, **15**, 12315-12326.

[15] D. L. Zhang, J. W. Zha, W. K. Li, C. Q. Li, S. J. Wang, Y. Q. Wen, Z. M. Dang, Compos. Sci. Technol., 2018, **156**, 1-7.

[16] T. Ma, Y. Zhao, K. Ruan, X. Liu, J. Zhang, Y. Guo, X. Yang, J. Kong, J. Gu, ACS Appl. Mater. Interfaces, 2020, **12**, 1677-1686.

[17] H. L. Lee, O. H. Kwon, S. M. Ha, B. G. Kim, Y. S. Kim, J. C. Won, J. Kim, J. H. Choi, Y. Yoo, Phys. Chem. Chem. Phys., 2014, **16**, 20041-20046. Z. Yang, L. H. Zhou, W. Luo, J. Y. Wan, J. Q. Dai, X. G. Han, K. Fu, D. Henderson, B. Yang, L. B. Hu, Nanoscale, 2016, 8, 19326-19333.

[18] H. Yuan, T. Li, Y. Wang, X. Wang, X. Zhang, B. Xia, P. Ma, T. Liu, M. Chen, W. Dong, Comp. Commun., 2021, **27**, 100851.

[19] J. He, J. Song, Y. Xu, X. Zhang, H. Zhou, W. Zhang, Y. Li, W. Yan, H. Ye, L. Xu, ACS Appl. Polym. Mater., 2023, **5**, 6232-6343.

[20] X. Wang, P. Wu, ACS Appl. Mater. Interfaces, 2018, **10**, 2504-2514.

[21] X. Shi, R. Zhang, K. Ruan, T. Ma, Y. Guo, J. Gu, J. Mater. Sci. Technol., 2021, **82**, 239-249.